This article has been accepted for publication in a future issue of this journal, but has not been fully edited. Content may change prior to final publication. Citation information: DOI 10.1109/TIA.2018.2849725, IEEE Transactions on Industry Applications

Investigation of Different Servo Motor Designs for Servo Cycle Operations and Loss Minimizing Control Performance

Huthaifa Flieh, Robert D. Lorenz
University of Wisconsin-Madison, WEMPEC
Madison, Wisconsin, USA
hflieh@wisc.edu , rdlorenz@wisc.edu

Eigo Totoki, Shinichi Yamaguchi, Yuichiro Nakamura
Mitsubishi Electric Corporation
Amagasaki city, Hyogo, Japan
Totoki.Eigo@dn.MitsubishiElectric.co.jp
Yamaguchi.Shinichi@dp.MitsubishiElectric.co.jp
Nakamura.Yuichiro@ak.MitsubishiElectric.co.jp

***Abstract*—Servo motors are widely used in many industrial applications. These motors require precise control of acceleration, speed, and position. Different designs can be found in the literature. This paper will compare the response of two common types and will propose a new servo motor design that uses less magnet, lowering the price of the motor. The proposed motor would be able to save energy for the required application (minimize cost industrial process cost) and would be suitable for high-frequency injection based self-sensing techniques.**

Keywords —Surface mounted permanent magnet synchronous motor (SPMSM), interior magnet permanent magnet synchronous motor (IPMSM), flux weakening (FW), flux intensifying (FI), field-oriented control (FOC), deadbeat-direct torque and flux control (DB-DTFC).

I. INTRODUCTION

Servo motors are widely used in industrial applications that require precise control of acceleration, speed, and position. They are used in industrial robots, rolling machines, printers, etc. Servo motors require high dynamic performance. Different types of servo motors are able to serve this purpose. Permanent magnet synchronous motors (PMSMs) tend to have a high power density and high efficiency, making them the most commonly used type of servo motors.

Different PMSM designs are used for servo applications, but the two main types are the surface PM (SPMSM) and the interior PM (IPMSM). Servo motor design is optimized to achieve very low levels of ripple and cogging torque [1]. For these reasons, an IPMSM servo motor generally has low reluctance torque (low saliency ratio). The main advantage of an IPMSM configuration compared to an SPMSM is that there is no need to use a sleeve for high-speed operation.

Standard IPMSMs have trackable saliency, which makes these motors suitable for injection based self-sensing control. On the other hand, Standard SPMSMs has a negligible saliency, which makes this kind of motors not suitable for self-sensing. Many researchers proposed modifying the SPMSM design to create a small saliency that can be used for self-sensing control. For example, in [2] the authors proposed using a ringed-pole SPMSM design to create saliency. In [3] , the authors proposed using a narrow tooth tip to utilize the zigzag leakage flux which creates a small saliency. However, the impact of these techniques on the motor power conversion was not evaluated.

The fluctuation of rare earth magnet prices in the past few years encouraged motor designers to design new motors with a smaller amount of magnetic material, reducing the price of the servo drive. Improving motor efficiency can help in reducing the industrial application operational cost.

Several PM motor designs were proposed for automotive applications, and those designs use less magnetic material in order to try to reduce the total cycle loss of the electrical drive. In [4] the authors propose using flux intensifying IPMSM (FI-IPMSM) structure for a variable gear electric vehicle drive. The authors use less magnetic material and add q axis flux barriers to invert the motor saliency. The authors of [5] propose an outer rotor FI-IPMSM. They claimed that their design could improve the torque under flux intensifying conditions and can operate for an extended speed range.

In [6] the authors compared the performance of self-sensing at very low-speed for flux weakening IPMSM (FW-IPMSM) and FI-IPMSM, they claimed that FI-IPMSM motor has better self-sensing performance than standard FW-IPMSM motors, They showed that FI-IPMSM achieves higher efficiency during high-speed operation, but with lower peak torque compared to standard FW-IPMSM, which reduces total cycle loss in duty cycle traction application.

Flux intensifying PM motors that can achieve the desired peak, cogging and ripple torque requirements for servo applications have not been reported in the literature.

Many comparisons between SPMSM and IPMSM designs are found in the literature, conducted in machines for traction applications without considering the ripple and cogging torque. For example, in [7], the authors designed two motors, SPMSM and IPMSM, that satisfy the traction requirements. Both machines achieve similar performance. However, the SPMSM has a shorter stack length and lower rated current compared to the IPMSM motor (SPMSM would have higher back-EMF for the same stack length). A similar comparison was found in [8]. The comparison was performed in high-speed machines for automotive applications. A retaining sleeve is used in case of the SPMSM. This sleeve might not be required in the case of small size servo motors.

This article has been accepted for publication in a future issue of this journal, but has not been fully edited. Content may change prior to final publication. Citation information: DOI 10.1109/TIA.2018.2849725, IEEE Transactions on Industry Applications

A fair comparison between SPMSM and IPMSM for servo applications with very low ripple and cogging torque has not been reported in the literature.

In this paper, the SPMSM and IPMSM motors will be fairly compared. The two motors were designed using the same stator, magnet, and airgap length while satisfying the servo application requirements. Then, a new servo motor design will be presented, called flux intensifying SPMSM (FI-SPMSM). This design uses less magnet material and its variable flux features can be used to save a significant amount of energy during the servo cycle operation. This design is also suitable for injection-based self-sensing, unlike standard SPMSMs.

Section II of this paper will present a brief introduction to servo applications and servo cycles. Section III will show the finite element analysis (FEA) design procedure for both SPMSM and IPMSM rotors. Design methodology for FI-SPMSM rotor will be presented in this section. The performance of the three rotors using both FEA and experimental results will also be compared in this section.

Self-sensing properties of the designed FI-SPMSM motor is discussed in section IV. Section V will show the energy loss for different servo cycles for the three motors. Finally, conclusions about this paper will be summarized.

II. Servo Applications and Servo Cycles

To achieve the required servo performance, motor designers try to design servo motors with very low cogging and ripple torque [9]. Table I summarizes typical ripple and cogging torque requirements for servo applications. Due to the extra ripple and cogging torque that is caused by manufacturing process variations, the simulated ripple and cogging torque using FEA needs to be lower than the specified requirements in Table I [10]. In general, servo applications can be categorized into two main groups: point-to-point servo cycles and continuous operational servo cycles.

Table I: Servo motor application requirements

Specification	Requirement
cogging torque	<1.5% rated torque
torque ripple	<4% rated torque

Point-to-point servo cycles or pick-and-place servo cycles are used in different applications like robots, printers, CNC machines, etc. the time span of these kinds of cycles is short, often only a few seconds. Servo motor used in these kinds of cycles require precise position control at both starting and ending points.

Continuous operational servo cycles are used in applications that require precise position and speed control all the time, it is used in rolling machines, aluminum foil manufacturing machines, painting robots, etc.; the time span for these kinds of cycles is longer than point-to-point cycles, typically measured in minutes. Figure 1-a shows a sample of a point-to-point cycle, while Fig1-b shows a sample of continuous operational servo cycle. In this paper, continuous operational servo cycles will be studied. Energy loss in these cycles will be compared for different servo motor designs.

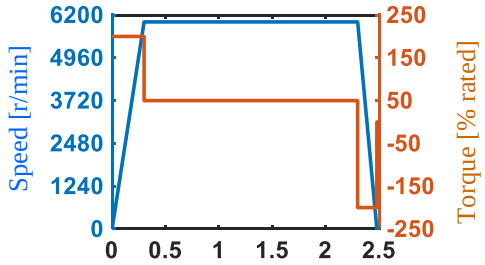

(a) point-to-point cycle

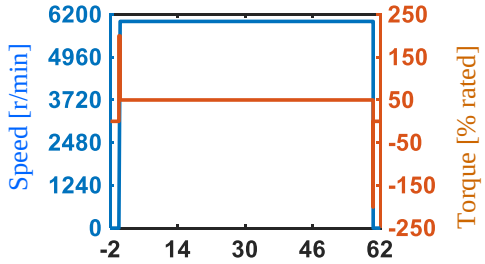

(b) continuous operational cycle

Fig. 1 Examples of servo cycles:
point-to-point cycle and continuous operational cycle

III. Design of Different PM Servo Motor Rotors using Finite Element Analysis

The general SPMSM sizing equations found in [11], [12], [13], and [14].were used to obtain the initial design parameters. The airgap length is fixed at 0.4 mm (smallest feasible length). 12 slots and 10 poles configuration is selected to achieve high winding factor (0.966) and low cogging torque [15]. Bread-loaf magnet with parallel magnetization pattern is used in this motor, this helps in achieving a very small cogging and ripple torque [16],[17]. Table II summarizes the main characteristics and dimensions for the designed SPMSM.

Table II: SPMSM baseline motor specifications

Specification	Value	Specification	Value
rated power	750 W	stator inner diameter	43 mm
rated torque	2.387 Nm	stator outer diameter	76.4 mm
rated speed	3000 r/min	max speed	6000 r/min
number of poles	10	number of slots	12
airgap length	0.4 mm	calculated BEMF	108 V(peak)
stack length	45 mm	rated current –rms	3.29 A

2D-FEA using JMAG™ Designer software was used to get the final design parameters for the SPMSM. The magnet in this motor is shaped to achieve a very low cogging and ripple torque. Figure 2-a shows a cross-sectional view of the designed rotor. After that, an IPMSM rotor was designed; this rotor uses the same magnet as the SPMSM rotor to reduce the manufacturing cost of this prototype rotor. To achieve low cogging and ripple torque performance, a flower shaped IPMSM rotor configuration was used.

This article has been accepted for publication in a future issue of this journal, but has not been fully edited. Content may change prior to final publication. Citation information: DOI 10.1109/TIA.2018.2849725, IEEE Transactions on Industry Applications

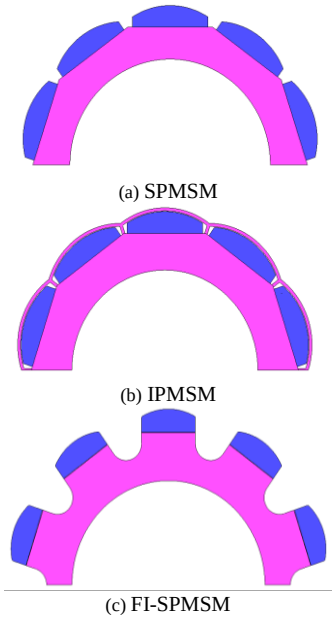

(a) SPMSM

(b) IPMSM

(c) FI-SPMSM

Fig. 2 Cross-sectional view of rotor design for SPMSM, IPMSM, and FI-SPMSM

The airgap of the flower shaped IPMSM motor is not uniform (this achieves similar reluctance in both d.q axis directions). This is done through adding a 0.4 mm around the magnet. Figure 2-b shows a cross-sectional view of this rotor. This configuration minimizes the leakage flux compared to the circular rotor IPMSM, which improves the torque production of the motor. Figure 3 compares the flux lines for the flower shaped rotor IPMSM with the circular shaped rotor IPMSM. The circular shaped IPMSM has larger leakage flux, this reduces the back-EMF of this motor by 18% as in Fig. 4-a.

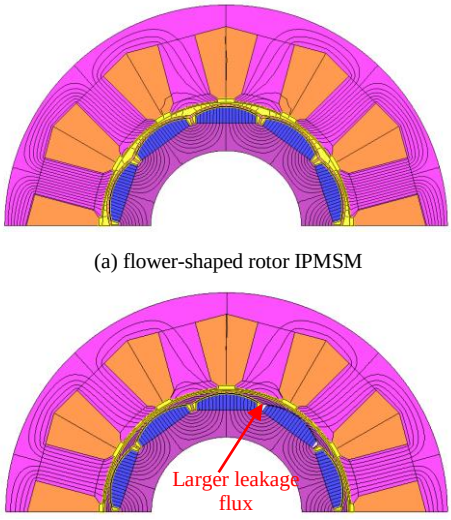

(a) flower-shaped rotor IPMSM

(b) circular-shaped rotor IPMSM

Fig. 3 Cross-sectional view and flux lines for IPMSM using flower and circular shaped rotors

Flower shaped IPMSM configuration helps in reducing the back-EMF harmonics and achieving low ripple and cogging torque (meet the servo requirements), The flower shaped rotor IPMSM has lower back-EMF harmonics as shown in Fig4-d. This motor achieves significantly lower cogging torque compared to the circular shaped rotor IPMSM motor as shown in Fig.4-b. Adding the thin iron layer on top of the magnet in the flower shaped IPMSM design reduces the airgap flux density by 10% compared to the SPMSM design. This can be seen from Fig.5-a and Fig.5-b; the peak torque in the IPMSM is 10% lower than the SPMSM. This happens due to the airgap flux reduction in this motor. This difference is also shown in the measured back-EMF waveform as in Fig.12.

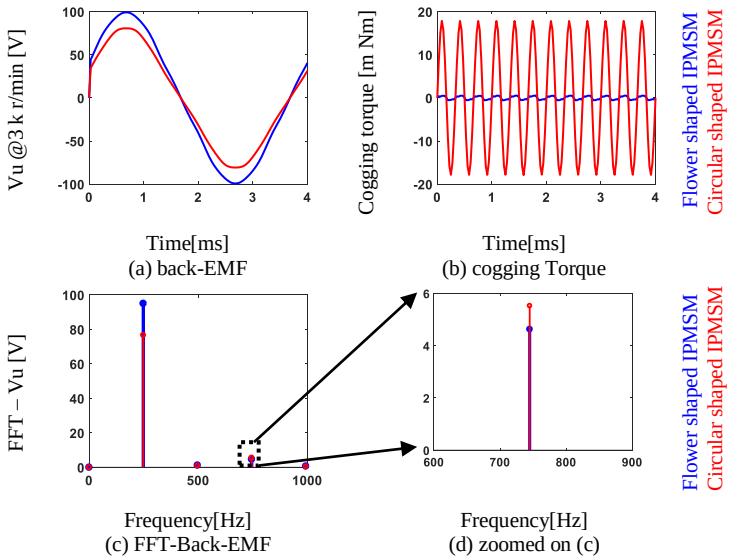

Fig. 4 Performance comparison between flower-shaped rotor IPMSM and circular-shaped rotor IPMSM

Figure 5-a shows the obtained efficiency map while Fig. 5-d shows the iron loss map for the SPMSM. These results were obtained by using a set of correction factors that were obtained from designing a similar motor and through comparing 2D with 3D FEA simulations. These factors are summarized in Table III. These factors were used to consider the effect of end winding, and leakage flux to reduce the simulation time (without using 3D FEA to generate the maps). The efficiency and iron loss maps for the IPMSM motor are shown in Fig. 5-b and Fig. 5-e, respectively.

Table III: Correction factors used with 2D-FEA

Specification.	Correction factor
airgap flux density (SPMSM, IPMSM)	0.9
airgap flux density (FI-SPMSM)	0.965
inductance (SPMSM, IPMSM)	1.3
inductance (FI-SPMSM)	1.2
iron loss	2

The airgap flux density correction factor is obtained by comparing the calculated back-EMF from 2D-FEA with 3D-FEA simulations with modeling the end winding. The inductance correction factor is used to add the leakage inductance to the 2D calculated inductance. This factor is calculated by comparing 2D-FEA with 3D-FEA simulations. The iron loss correction factor was found by measuring the iron loss for a similar motor with the same materials (at different speed and torque conditions) and compare it with the estimated loss from the 2D-FEA.

This article has been accepted for publication in a future issue of this journal, but has not been fully edited. Content may change prior to final publication. Citation information: DOI 10.1109/TIA.2018.2849725, IEEE Transactions on Industry Applications

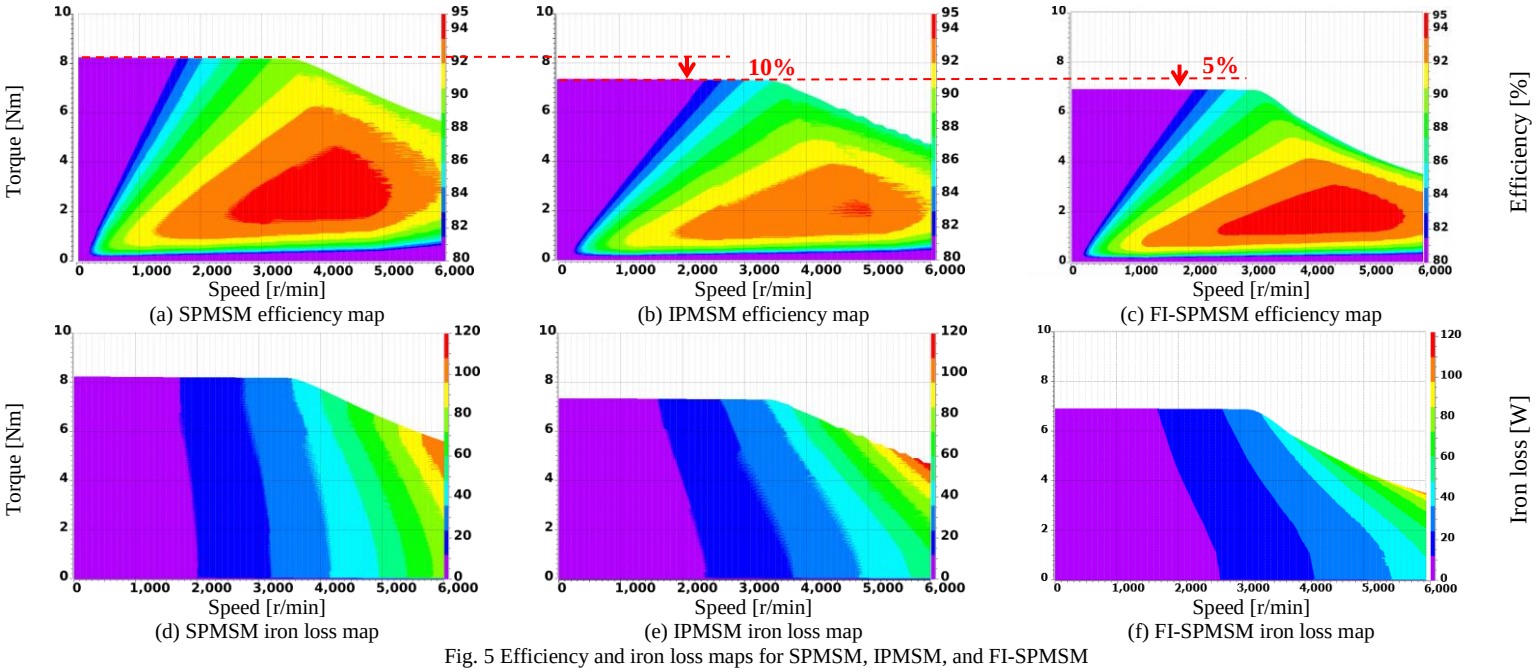

Fig. 5 Efficiency and iron loss maps for SPMSM, IPMSM, and FI-SPMSM

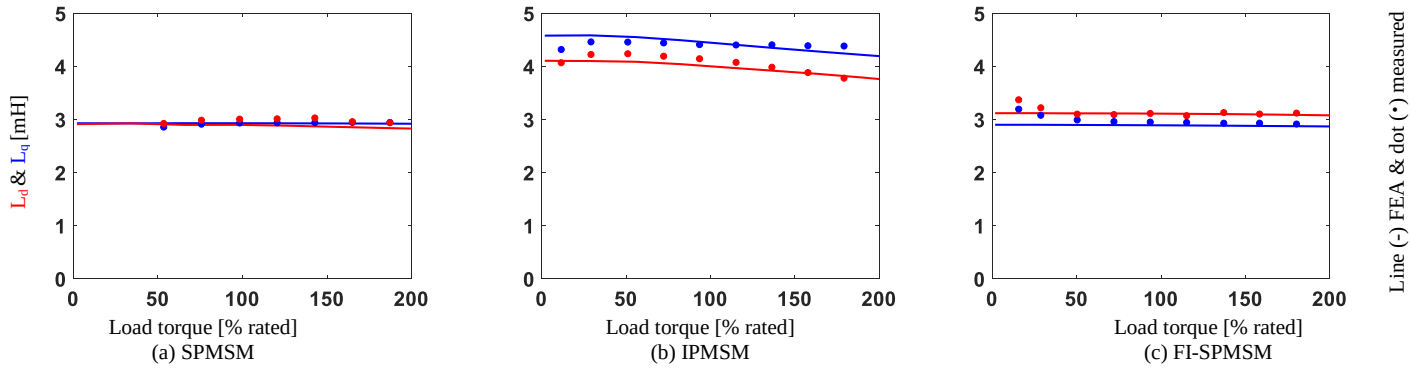

Fig. 6 Measured and simulated inductance variation with load condition for SPMSM, IPMSM, and FI-SPMSM

JMAG software uses the above correction factors to adjust the current phase and amplitude, then the corresponding loss for that current is obtained from the loss lookup tables that are generated based on FEA. Iron loss correction factor is used to adjust the iron loss coefficients that are already programmed in JMAG. More information about this process can be found in JMAG-RT help tool.

Using an SPMSM structure will maximize the air-gap flux density per magnet volume, achieving larger peak torque compared to the IPMSM configuration as in Fig.5-a and Fig.5-b. Comparing Fig. 5-d and Fig. 5-e, IPMSM rotor has lower iron loss during high-speed operation, this is due to the lower air-gap flux density compared to the SPMSM rotor. IPMSM rotor has a small saliency ratio around 11%. (this is a flux weakening motor with $L_q>L_d$ [6]), This saliency is useful for self-sensing purposes, while the SPMSM has a negligible saliency, which makes it unsuitable for self-sensing purposes. Figure 6-a shows the variation of inductance with respect to the load condition for the SPMSM rotor while Fig. 6-b shows the same results for the IPMSM rotor. This figure also compares the measured inductances with estimated values using 2D-FEA with correction factors. Both results show a good agreement which verifies the used correction factors.

Combining the benefits of both IPMSM and SPMSM is possible through properly designing the FI-SPMSM. The design procedure for the FI-SPMSM is similar to designing the FI-IPMSM as in [5] and [6], in which the airgap flux is reduced. With that, a lower iron loss is achieved during high-speed operation, and a lower negative d axis current is required to weaken the flux when the motor operating at the inverter voltage limit during high-speed operation. By adding q axis flux barriers, an inverted saliency ($L_d>L_q$) is introduced to the motor. This saliency is helpful for both self-sensing purposes and for boosting the airgap flux linkage during the peak torque operation.

Analytical equations for designing an SPMSM are still valid for the case of the FI-SPMSM. In this paper, the fundamental airgap flux density of the SPMSM was reduced by decreasing the magnet span from 162° to 110° electrical degree using (1). This is done to reduce the flux weakening

This article has been accepted for publication in a future issue of this journal, but has not been fully edited. Content may change prior to final publication. Citation information: DOI 10.1109/TIA.2018.2849725, IEEE Transactions on Industry Applications

current during the high-speed operation (6000 r/min) to zero, which improves high-speed efficiency. This was done using the first harmonic assumption; Figure 8 shows the reduction of the fundamental airgap flux density by reducing the magnet span. This will reduce the motor back-EMF at 6000 r/min from 190 V_{Φ_peak} to 165 V_{Φ_peak}. The maximum voltage provided by the inverter is 120 V_{peak} (this is limited by the inverter DC link voltage).

$$B_g = \frac{4}{\pi} \bullet B_m \bullet \sin(\alpha) \quad (1)$$

where: 2α = magnet span (degree) corresponds to τ_m as shown in Fig. 7,

B_m = PM flux density (tesla)

B_g = airgap flux density (tesla)

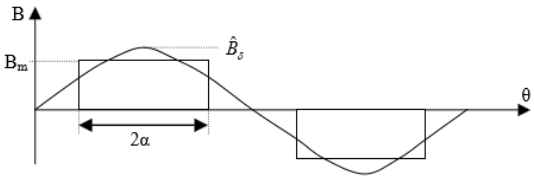

Fig. 7 Quasi-square wave and fundamental airgap flux

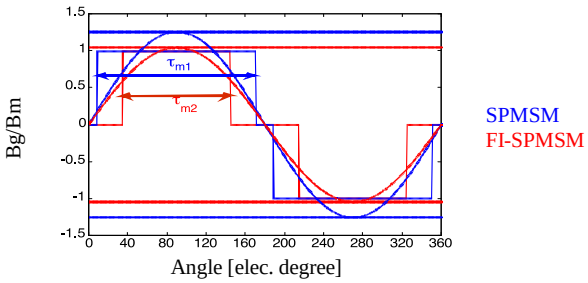

Fig. 8 Magnet span reduction to reduce the fundamental air-gap flux

After reducing the fundamental air-gap flux (through reducing the magnet span), an enough inverted saliency ratio (Ld > Lq) is added to the motor. This is done by optimizing the q axis flux barriers and by shaping the magnet to achieve the desired cogging and ripple torque.

Multi-objective optimization using genetic algorithm was done using Matlab™ optimization engine with JMAG™ Designer software. 30 generations with 10 population size were used. The optimization engine ran 273 cases to find the optimum solution, for every case the current was set to zero to measure the cogging torque and to the rated current to measure the average and ripple torque, while the motor is spinning at 3000 r/min.

The optimization objectives were set to maximize the saliency ratio (L_d / L_q), maximize the average torque, limiting the cogging torque to be less than 0.52%, and limiting the torque ripple to be less than 3%. Figure 9 indicates the parameters varied during the optimization process, the varied range is shown in Table IV.

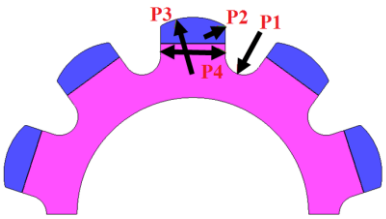

Fig. 9 Varied geometry during optimization process for FI-SPMSM rotor

Table IV: Varied parameters during the optimization process

Parameter	Range
q-axis flux barrier radius (p1)	1 - 2.2 mm
magnet fillet radius (p2)	0.25-1.5 mm
magnet outer radius (p3)	5 - 15 mm
magnet span (p4)	5-8 mm

Figure 2-c shows the cross-sectional view of the optimized FI-SPMSM rotor, while Fig. 5-c and Fig. 5-f show the efficiency and iron loss maps for this motor. This configuration has 15% lower peak torque compared to SPMSM, and 5% lower peak torque compared to the IPMSM. This is due to using a lower amount of magnet material but will achieve the required torque during the studied servo cycles (2 times the rated torque is required during the peak acceleration period). The FI-SPMSM has a significantly lower iron loss compared to both SPMSM and IPMSM rotors, which makes this motor very efficient during medium and high-speed operation. Figure 6-c shows the inductance variation for the FI-SPMSM with load variations. This motor has an inverted saliency ratio, around 10%. This saliency ratio would be useful for self-sensing purposes.

The designed FI-SPMSM uses only 64% of the magnet volume used in SPMSM or IPMSM, this will decrease the manufacturing cost of this motor from 7-10 % (magnet cost for this size of motors is around 20-30% the total cost). This motor has slightly higher torque ripple and cogging torque compared to the SPMSM and IPMSM, but still meets the servo requirements. Table V compares the performance of the three motors using FEA and experimental evaluation.

Table V: Comparisons between the three designed motors

Specification	SPMSM	IPMSM	FI-SPMSM
back-EMF voltage @3000 r/min (peak phase)	95V	86.5V	82.2V
PM flux (measured)	0.0623 Wb	0.0556 Wb	0.0529 Wb
rated current (measured)	3.63 A_{rms}	3.99 A_{rms}	4.2 A_{rms}
rated torque (measured)	2.38 N.m	2.38 N.m	2.38 N.m
magnet volume (FEA)	100%	100%	64%
torque ripple (FEA)	1.1%	2.5%	2.8%
cogging torque (FEA)	0.3 %	0.35%	0.51%
Saliency ratio (measured)	≈0	11%	10% (inverted)

FI-SPMSM has 15% higher rated current compared to the SPMSM, and 5% higher rated current compared to the IPMSM motor, thus this motor will have higher losses during the low-speed high torque operations when the motor copper loss is dominant. However, servo motors run at the peak torque only for a very short period during acceleration, then run at high speed with partial load. Since the FI-SPMSM has a

This article has been accepted for publication in a future issue of this journal, but has not been fully edited. Content may change prior to final publication. Citation information: DOI 10.1109/TIA.2018.2849725, IEEE Transactions on Industry Applications

significantly lower iron loss during the high-speed operation this motor can achieve a lower total motor cycle loss during the high-speed servo cycles.

In this paper, the same stator was used for evaluating the three different rotors. Figure 10 shows the designed stator which is a double layer concentrated winding.

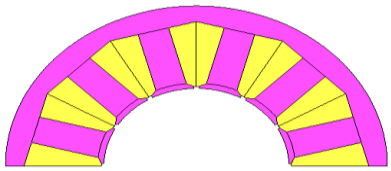

Fig. 10 The designed stator

Figure 11 shows the fabricated rotors, while Fig. 12 compares the simulated back EMF using 2D-FEA, 2D-FEA with considering the correction factors and the measured one for the three rotors. The measured results match with the expected results from the FEA simulation.

Fig. 11 The fabricated rotors
(left) SPMSM (center) IPMSM (right)FI-SPMSM

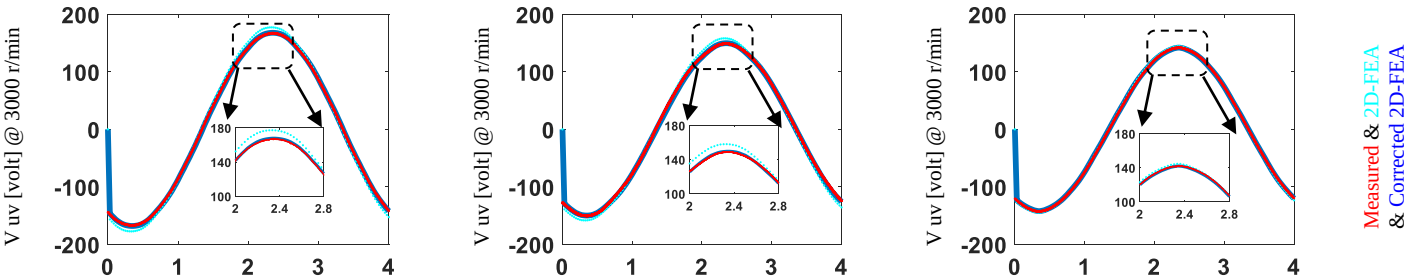

(a) SPMSM (b) IPMSM (c) FI-SPMSM

Fig. 12 Simulated and measured back EMF voltage for SPMSM, IPMSM, and FI-SPMSM

FI-SPMSM motor has a lower magnet leakage flux in the axial direction compared to both IPMSM and SPMSM rotors. This is due to using a shorter magnet span in the FI-SPMSM motor (larger gap between the magnets with larger reluctance). In the previous analysis, both SPMSM and IPMSM rotors have approximately a 10% total leakage flux. However, FI-SPM motor has only 3.5% total leakage-flux. This number is obtained by comparing the measured back-EMF with the 2D FEA simulations.

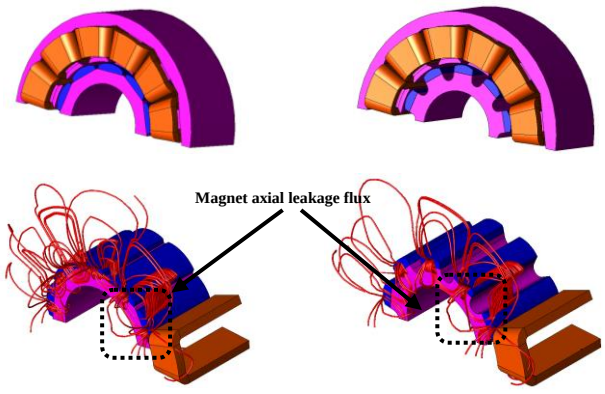

(a) SPMSM (b) FI-SPMSM

Fig. 13 3D model and axial magnet leakage flux for SPMSM and FI-SPMSM

Figure 13 shows the reluctance path for the axial leakage flux from the magnet for both SPMSM and FI-SPMSM, the air reluctance in the axial direction for the SPMSM is smaller (magnet span is short), while in the case of the FI-SPMSM, the air reluctance in the axial direction is larger (larger distance between the magnets). This leads to lower magnet leakage flux in the axial direction for the FI-SPMSM compared to the SPMSM.

To explore the benefits of the q axis flux barriers in the proposed FI-SPMSM rotor, the flux barriers partially filled with iron (same rotor structure like the SPMSM rotor), and the flux barriers filled with iron (inset SPMSM structure) is used as in Fig.14. Using the SPMSM rotor iron with the FI-SPMSM magnet achieves similar average torque, this motor has an inverted very small saliency (this motor has FI properties), while shaping the flux barriers in the FI-SPMSM rotor improves the saliency allowing using it for self-sensing purposes. Figure 15 compares the saliency ratio for these two motors at different load conditions.

This article has been accepted for publication in a future issue of this journal, but has not been fully edited. Content may change prior to final publication. Citation information: DOI 10.1109/TIA.2018.2849725, IEEE Transactions on Industry Applications

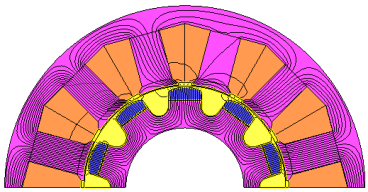

(a) FI-SPMSM

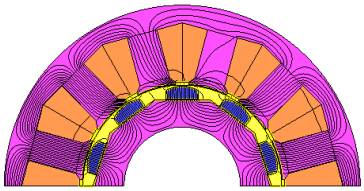

(b) SPMSM rotor iron with FI-SPMSM Magnet

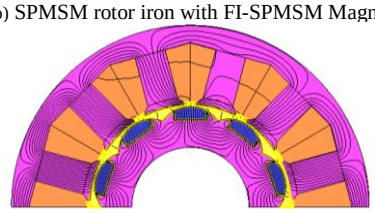

(c) inset SPMSM

Fig. 14 Cross-sectional view of FI-SPMSM, SPMSM with a shorter magnet span and inset SPMSM

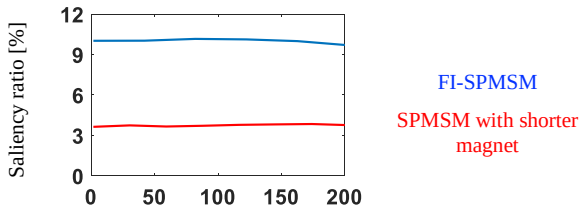

Fig.15 Saliency ratio comparison between FI-SPMSM and SPMSM with shorter magnet span

The FI-SPMSM rotor is then converted to an inset SPMSM rotor through adding iron between the magnets as in Fig. 14-c. The iron between the magnets provided a path for the flux to leak, affecting the torque production of the motor and decreasing the average torque by 6.6%. Figure 16 compares the average torque for the two motors using the same excitation current.

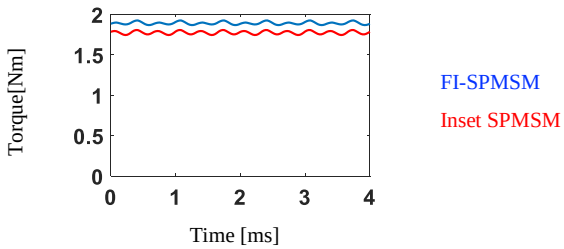

Fig.16 Average torque comparison between FI-SPMSM and inset SPMSM

IV. Self-Sensing Properties of the Designed FI-SPMSM

Self-sensing techniques are useful methods to control the motor without any physical position sensor, through using the motor itself as a sensor. This improves the reliability of the drive and decreases the drive physical size and cost. Two main self-sensing techniques are used in the literature; the first one is effective for medium and high-speed operation through tracking the motor back-EMF. This method works for all electromagnetic machine types [18].

The other self-sensing technique is used to control the motor during zero and low-speed operations. This is done through tracking the motor saliency, which can be tracked by injecting a high-frequency signal on top of the fundamental voltage and estimate the rotor position form the measured motor current without using position sensor [19]. This method is effective in salient motors like IPMSM, however, applying these techniques to SPMSM requires designing the motor for that purpose [2].

The FI-SPMSM is designed to have good self-sensing performance during zero and low-speed operation. The dq axis inductances are almost fixed with load variations. In this case, no massive inductance lookup tables are required for self-sensing control [20].

Figure 17 shows the FI-SPMSM saliency image at different load conditions at zero speed. This image is obtained through exciting the FEA motor model with a high frequency rotating current vector, then observing the high-frequency stator flux linkage. The motor saliency image has an elliptical shaped that rotates with the motor rotor. Motor position can be estimating through comparing the observed ellipse with a pre-defined template, this method is called image tracking self-sensing control [21]. FI-SPMSM saliency image is fixed with load variations; this simplifies the image template for image tracking self-sensing control, in which one template can be used at different load conditions.

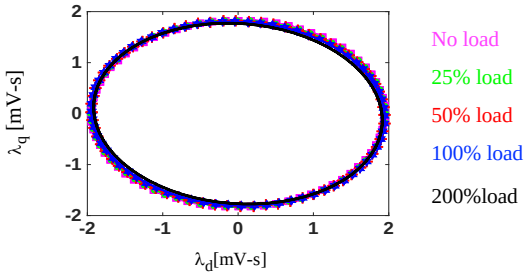

Fig.17 Saliency image of FI-SPMSM at different load conditions

The accuracy of the injection based self-sensing technique depends also on the angular offset of the saliency image at different load conditions [22], this happens due to the cross-saturation effect between the d and q axis. The angular offset of the designed FI-SPM motor is less than 2 electrical degrees at 200% load, which can be ignored in many applications without the need for compensation lookup table to decouple its effect. Figure 18 shows the angular offset at different load conditions). The results of self-sensing control for the FI-SPMSM motor will be presented in future publications.

This article has been accepted for publication in a future issue of this journal, but has not been fully edited. Content may change prior to final publication. Citation information: DOI 10.1109/TIA.2018.2849725, IEEE Transactions on Industry Applications

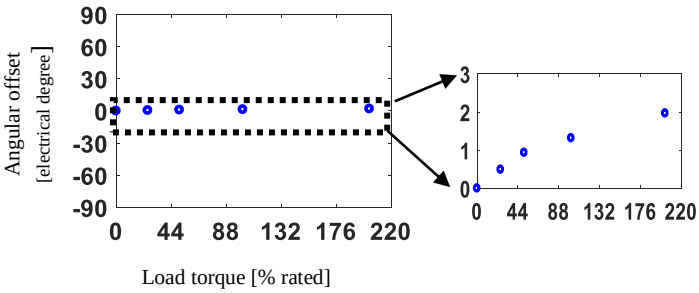

Fig.18 Angular offset of FI-SPMSM saliency image at different load conditions

V. Servo Cycle Loss Evaluation and Comparison of The Designed Three Motors

In this section, the energy loss in different servo cycles was measured and compared for the three fabricated rotors. In order to do so, the tested motor was connected to a commercial 3 HP servo motor through a torque sensor. Figure 19 shows the used dynamometer. A motor drive analyzer (MDA 810 from Teledyne LeCroy) was used to measure the tested motor loss.

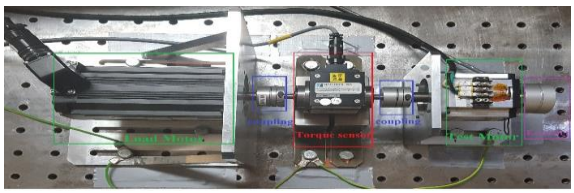

Fig. 19 The dynamometer test setup

The load motor was controlled using a field-oriented controller (FOC), while the tested motor was in motion control using loss minimizing control in deadbeat-direct torque and flux control (LMC-DB-DTFC). This controller controls the motor to operate at the optimum operating condition. More details about this controller are discussed in [23].

To evaluate the energy loss during acceleration and deceleration, the dynamic shaft torque signal is used to measure the mechanical motor power. This signal is obtained from a dynamic shaft torque observer, more details about this observer can be found in [24].

To understand the performance of the three motors a simplified servo cycle is evaluated for the three motors. Figure 20-a shows the calculated speed from the encoder for the three motors, while Fig. 20-b shows the dynamic shaft torque signal during this experiment.

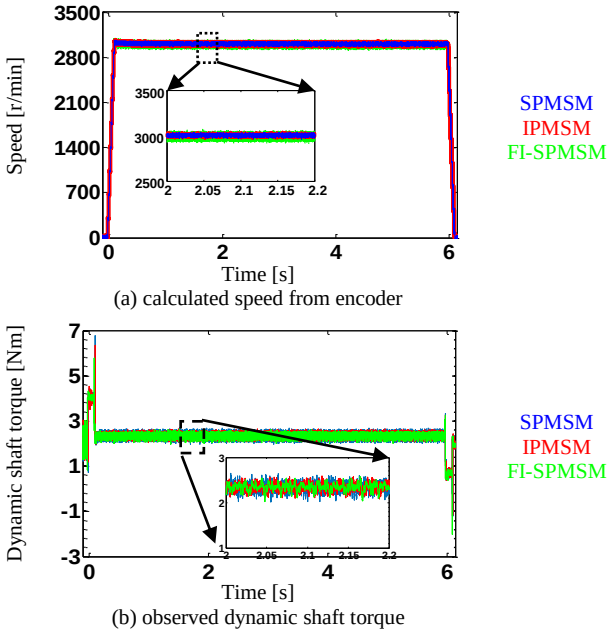

(a) calculated speed from encoder

(b) observed dynamic shaft torque

Fig. 20 Calculated speed from the encoder and estimated dynamic shaft torque for the studied simple servo cycle for the three motors

Figure 21 compares the measured dq axis currents for the three motors for the studied cycle. SPMSM requires lower q axis current to generate the same torque compared to both IPMSM and FI-SPMSM, this is because this motor has the highest magnet flux (highest airgap flux density). However, IPMSM has a very close current to the FI-SPMSM. FI-SPMSM requires 15% higher current during the acceleration period. Since this period is very short (150-300 ms), the same size inverter can be used (inverter can be overloaded for such short periods).

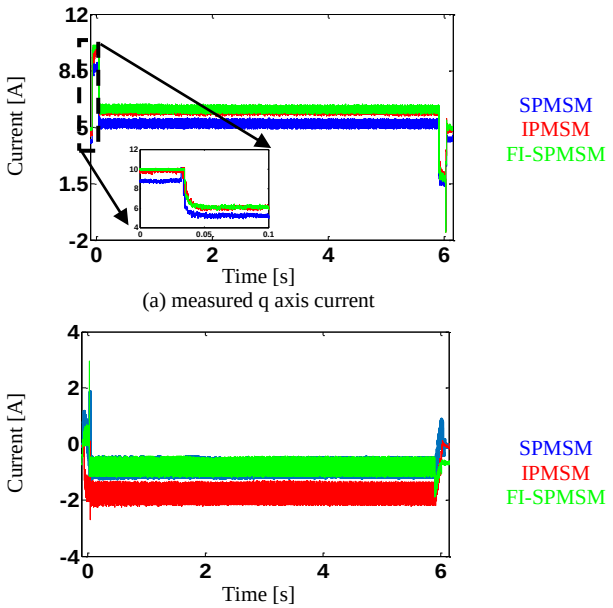

(a) measured q axis current

(b) measured d axis current

Fig. 21 Measured dq axis current for the studied simple cycle for the three motors

This article has been accepted for publication in a future issue of this journal, but has not been fully edited. Content may change prior to final publication. Citation information: DOI 10.1109/TIA.2018.2849725, IEEE Transactions on Industry Applications

IPMSM optimum d axis current during the 3000 r/min operation is higher than both SPMSM & FI-SPMSM, to reduce the total motor loss. Both SPMSM & FI-SPMSM have similar d-axis currents, however, running the motor at a higher speed will cause the SPMSM to command a more negative d axis current to weaken the flux when it is operating at the voltage limit. During this operation, The FI-SPMSM will achieve a lower copper loss.

Figure 22 shows the estimated stator flux linkage for the three motors during the same cycle. FI-SPMSM has lower stator flux linkage than the other motors, which means lower iron loss.

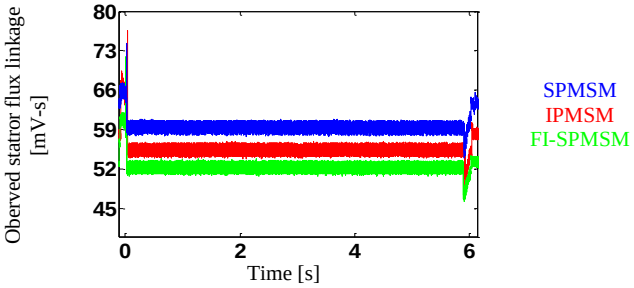

Fig. 22 Estimated stator flux linkage from the flux observer for the studied simple cycle for the three motors

Figure 23 compares the measured loss for the three motors over the short cycle. For this cycle, the copper loss dominates the loss. For this reason, the FI-SPMSM has 28% higher losses than the SPMSM and 5% lower losses than the IPMSM.

The iron loss was measured by subtracting total motor loss from copper loss (Friction and windage losses are negligible for small size motor).

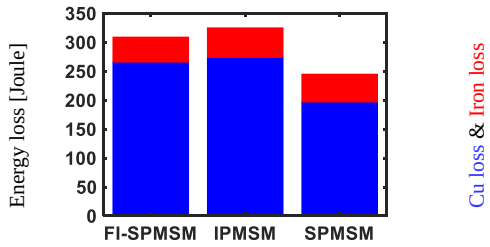

Fig. 23 Measured loss for the three rotors for the 3000 r/min short cycle

Figures 24, 25 and 26 evaluate three continuous operational servo cycles. In the first cycle, the tested motor was accelerated from 0 to 3000 r/min in 150 ms, then the motor ran at 3000 r/min for 60 seconds. During this cycle, the rated torque (2.4 Nm) is applied using the load motor. 200% of the rated torque was applied to the tested motor during the acceleration period. Loss comparison for this cycle is shown in Fig. 24. Similar to the short cycle, copper loss dominates the cycle loss. In this case, FI-SPMSM has 28% higher losses than SPMSM and 5% lower than IPMSM.

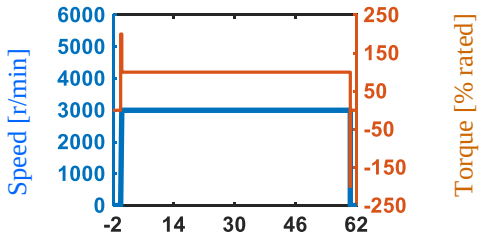

(a) 3000 r/min continuous servo cycle

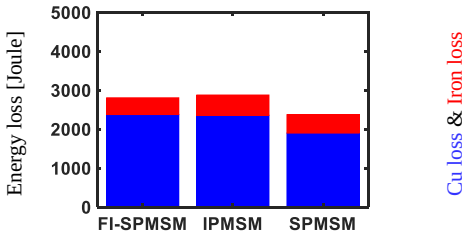

(b) measured energy loss

Fig. 24 Measured loss of the three rotors for 3000 r/min continuous servo cycle

In the second evaluated cycle, the tested motor was accelerated from 0 to 4000 r/min in 200 ms, then the motor ran at 4000 r/min for 60 seconds. During this cycle, 1.8 Nm (74% rated torque) load torque was applied using the load motor. 200% of the rated torque was applied on the tested motor during the acceleration period. The copper loss for FI-SPMSM is higher than the copper losses for the SPMSM. This is because the FI-SPMSM has lower magnet flux, so more current is required to produce the required torque. However, the iron loss is significantly lower in the FI-SPMSM compared to both the SPMSM and IPMSM. For this cycle, the FI-SPMSM has 32% lower energy loss compared to the SPMSM, and 16.5% lower energy loss compared to the IPMSM; the results of this experiment are shown in Fig. 25.

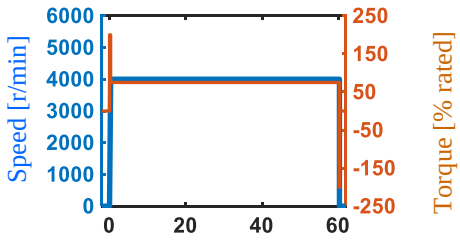

(a) 4000 r/ min continuous servo cycle

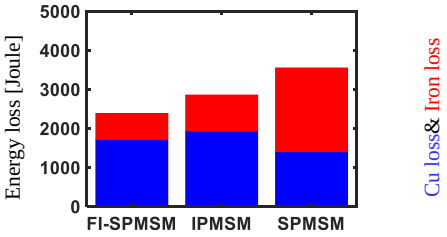

(b) measured energy loss

Fig. 25 Measured loss of the three rotors for 4000 r/min continuous servo cycle

This article has been accepted for publication in a future issue of this journal, but has not been fully edited. Content may change prior to final publication. Citation information: DOI 10.1109/TIA.2018.2849725, IEEE Transactions on Industry Applications

Figure 26 shows the results for the third evaluated cycle. In this cycle, the tested motor was accelerated from 0 to 4500 r/min in 225 ms, then the motor ran at 4500 r/min for 60 seconds. During this cycle, 1.6 Nm (66% rated torque) load torque was applied using the load motor. 200% of the rated torque was applied on the tested motor during the acceleration period. Like the previous cycle, FI-SPMSM has 40% lower energy loss compared to the SPMSM, and 20% lower energy loss compared to the IPMSM.

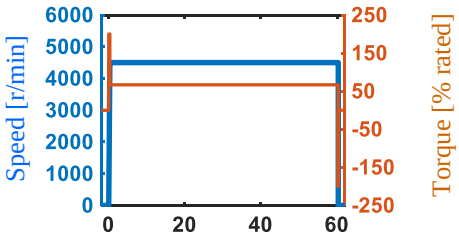

(a) 4500 r/min cycle

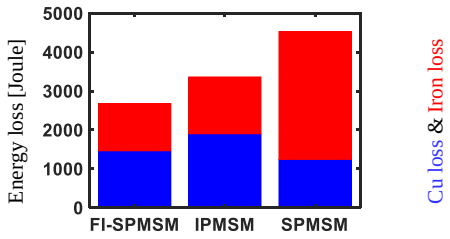

(b) measured energy loss

Fig. 26 Measured loss of the three rotors for 4500 r/min continuous servo cycle

In previous cycles, the three motors were not operating at the voltage limit. It is expected to save more energy for higher speed cycles that operate at the voltage limit because a lower negative d-axis current is required to weaken the flux during the high-speed operation using FI-SPMSM compared to the SPMSM. 6000 r/min servo cycle (the desired cycle) was not evaluated due to encoder speed limitations (maximum speed of the encoder was 4500 r/min).

VI. Conclusions

This paper presents a new servo motor design that uses less magnet material compared to the standard designs. The proposed design is called the FI-SPMSM, this design has a significantly lower loss for high-speed servo cycles.

The following conclusions can be reached from the results of this paper:

- SPMSM maximizes the airgap flux density per magnet volume. While IPMSM has lower airgap flux compared to the SPMSM, this motor achieves lower iron loss during the high-speed operation and has trackable saliency that can be used for self-sensing control.
- Flower shaped IPMSM rotor is an effective structure to reduce the magnet leakage flux in IPMSM while satisfying the servo requirements.
- The proposed FI-SPMSM combines the benefits of both SPMSM and IPMSM configurations. It maximizes the airgap flux density per magnet volume like an SPMSM, and it has low iron loss and detectable saliency like an IPMSM.
- The proposed FI-SPMSM uses only 64% of the magnet volume in the SPMSM, this significantly reduces the manufacturing cost of this motor.
- Copper loss dominates the cycle loss for low-speed high torque cycles. In these kinds of cycles, SPMSM motor will have the lowest cycle loss.
- Iron loss becomes significant for high speed, low torque cycles. In this case, FI-SPMSM will have the lowest losses compared to SPMSM and IPMSM.
- A significant amount of energy could be saved during high-speed continuous operational servo cycles if the proposed FI-SPMSM is adopted. The proposed rotor structure could save more energy for higher speed cycles when the motor is running at voltage limit operation.
- The decreased thermal loading (lower cycle energy loss) could be used to enable faster acceleration or to downsize the machine, both of which are very useful outcomes for servo motor applications.

Acknowledgment

The author wishes to acknowledge the motivation and support provided by the Wisconsin Electric Machines and Power Electronics Consortium (WEMPEC) of the University of Wisconsin-Madison, and Mitsubishi Electric Corporation, Japan.

References

[1] R. Krishnan, "Selection Criteria for Servo Motor Drives," in *IEEE Transactions on Industry Applications*, vol. IA-23, no. 2, pp. 270-275, March 1987.

[2] A. Faggion, N. Bianchi and S. Bolognani, "Ringed-Pole Permanent-Magnet Synchronous Motor for Position Sensorless Drives," in *IEEE Transactions on Industry Applications*, vol. 47, no. 4, pp. 1759-1766, July-Aug. 2011.

[3] S. C. Yang, T. Suzuki, R. D. Lorenz and T. M. Jahns, "Surface-Permanent-Magnet Synchronous Machine Design for Saliency-Tracking Self-Sensing Position Estimation at Zero and Low Speeds," in *IEEE Transactions on Industry Applications*, vol. 47, no. 5, pp. 2103-2116, Sept.-Oct. 2011.

[4] M.H.A. Prins, C.W. Vorster, M.J. Kamper, "Reluctance synchronous and field intensified-PM motors for variable-gear electric vehicle drives," *2013 IEEE Energy Conversion Congress and Exposition*, Denver, CO, 2013, pp. 657-664.

[5] B. Yan, X. Zhu, L. Chen, "Design and evaluation of a new flux-intensifying permanent magnet brushless motor," *2014 17th International Conference on Electrical Machines and Systems (ICEMS)*, Hangzhou, 2014, pp. 673-677.

[6] N. Limsuwan, Y. Shibukawa, D. D. Reigosa and R. D. Lorenz, "Novel Design of Flux-Intensifying Interior Permanent Magnet Synchronous Machine Suitable for Self-Sensing Control at Very Low Speed and Power Conversion," in *IEEE Transactions on Industry Applications*, vol. 47, no. 5, pp. 2004-2012, Sept.-Oct. 2011.

[7] P. B. Reddy, A. M. El-Refaie, K. K. Huh, J. K. Tangudu and T. M. Jahns, "Comparison of Interior and Surface PM Machines Equipped With Fractional-Slot Concentrated Windings for

Hybrid Traction Applications," in *IEEE Transactions on Energy Conversion*, vol. 27, no. 3, pp. 593-602, Sept. 2012.

[8] J. Dong, Y. Huang, L. Jin and H. Lin, "Comparative Study of Surface-Mounted and Interior Permanent-Magnet Motors for High-Speed Applications," in *IEEE Transactions on Applied Superconductivity*, vol. 26, no. 4, pp. 1-4, June 2016.

[9] P. Pillay and R. Krishnan, "Application characteristics of permanent magnet synchronous and brushless DC motors for servo drives," in *IEEE Transactions on Industry Applications*, vol. 27, no. 5, pp. 986-996, Sep/Oct 1991.

[10] J. Ou, Y. Liu, R. Qu and M. Doppelbauer, "Experimental and Theoretical Research on Cogging Torque of PM Synchronous Motors Considering Manufacturing Tolerances," in *IEEE Transactions on Industrial Electronics*, vol. 65, no. 5, pp. 3772-3783, May 2018.

[11] G. R. Slemon, "On the design of high-performance surface-mounted PM motors," in *IEEE Transactions on Industry Applications*, vol. 30, no. 1, pp. 134-140, Jan/Feb 1994.

[12] D.C. Hanselman, Brushless Permanent-Magnet Motor Design. 1st ed. New York: McGraw-Hill, 1994. Print.

[13] J.R Hendershot, T.J.E Miller. Design Of Brushless Permanent-Magnet Machines. 1st ed. Venice, Florida: Motor Design Books, 2010. Print.

[14] T.A. Lipo, Introduction To AC Machine Design. 1st ed. [Madison, Wis.]: Wisconsin Power Electronics Research Center, University of Wisconsin, 2004. Print.

[15] J. Cros and P. Viarouge, "Synthesis of high performance PM motors with concentrated windings," in *IEEE Transactions on Energy Conversion*, vol. 17, no. 2, pp. 248-253, Jun 2002.

[16] N. Bianchi and S. Bolognani, "Design techniques for reducing the cogging torque in surface-mounted PM motors," in *IEEE Transactions on Industry Applications*, vol. 38, no. 5, pp. 1259-1265, Sep/Oct 2002.

[17] S. Ruangsinchaiwanich, Z. Q. Zhu and D. Howe, "Influence of magnet shape on cogging torque and back-emf waveform in permanent magnet machines," *2005 International Conference on Electrical Machines and Systems*, 2005, pp. 284-289 Vol. 1.

[18] Zhiqian Chen, M. Tomita, S. Doki and S. Okuma, "An extended electromotive force model for sensorless control of interior permanent-magnet synchronous motors," in *IEEE Transactions on Industrial Electronics*, vol. 50, no. 2, pp. 288-295, Apr 2003.

[19] D. Raca, P. Garcia, D.D. Reigosa, F. Briz and R.D. Lorenz, "Carrier-Signal Selection for Sensorless Control of PM Synchronous Machines at Zero and Very Low Speeds," in *IEEE Transactions on Industry Applications*, vol. 46, no. 1, pp. 167-178, Jan.-feb. 2010.

[20] T. Zou, X. Han, D. Jiang, R. Qu and D. Li, "Inductance Evaluation and Sensorless Control of a Concentrated Winding PM Vernier Machine," in *IEEE Transactions on Industry Applications*, vol. 54, no. 3, pp. 2175-2184, May-June 2018.

[21] T.S. Slininger, Y. Xu and R.D. Lorenz, "Enhancing estimation accuracy by applying cross-correlation image tracking to self-sensing including evaluation on a low saliency ratio machine," *2016 IEEE Energy Conversion Congress and Exposition (ECCE)*, Milwaukee, WI, 2016, pp. 1-7.

[22] Ji-Hoon Jang, Seung-Ki Sul, Jung-Ik Ha, K. Ide and M. Sawamura, "Sensorless drive of surface-mounted permanent-magnet motor by high-frequency signal injection based on magnetic saliency," in *IEEE Transactions on Industry Applications*, vol. 39, no. 4, pp. 1031-1039, July-Aug. 2003.

[23] H. Flieh, R.D. Lorenz, E. Totoki, S. Yamaguchi and Y. Nakamura, "Dynamic loss minimizing control of a PM servomotor operating even at the voltage limit when using DB-DTFC," *2017 IEEE Energy Conversion Congress and Exposition (ECCE)*, Cincinnati, OH, USA, 2017, pp. 3604-3611.

[24] H. Flieh, E. Totoki and R.D. Lorenz, "Dynamic shaft torque observer structure enabling accurate transient loss measurements," *2017 IEEE International Electric Machines and Drives Conference (IEMDC)*, Miami, FL, 2017, pp. 1-8.

[25] H. Flieh, R. D. Lorenz, E. Totoki, S. Yamaguchi and Y. Nakamura, "Investigation of different servo motor designs for servo cycle operations and loss minimizing control performance," *2017 IEEE Energy Conversion Congress and Exposition (ECCE)*, Cincinnati, OH, 2017, pp. 4316-4323.